



Improved IVUS and VH-IVUS image segmentation using a hybrid approach based on active counter model and clustering algorithms

Zahra Rezaei¹

Received: 21 October 2023 / Revised: 7 June 2024 / Accepted: 10 June 2024

© The Author(s), under exclusive licence to Springer Science+Business Media, LLC, part of Springer Nature 2024

Abstract

Heart attack due to the vulnerable atherosclerotic plaque is one of the most common causes of death in the world. One of the imaging modalities in the coronary artery is Virtual Histology Intravascular Ultrasound (VH-IVUS); however, segmentation of overlapped plaque components can be challenging. Therefore, this research study proposes a new approach based on the level set method to detect the plaque border in VH-IVUS images accurately. Three classifiers, including support vector machine (SVM), k-nearest neighbor, and proposed Selecting Nearest Pixel (SNP), were hybridized with FCM to enhance the VH-IVUS segmentation. Moreover, for segmentation and plaque extraction in IVUS images, a hybrid of the snake approach and fuzzy clustering method is proposed. Geometric features were extracted from VH-IVUS and IVUS images. The proposed hybrid model used 599 images obtained from 10 patients. The validation for the proposed segmentation model showed an average of 0.96 for the silhouette validity index. The SVM classifier is used to classify the TCFA and Non-TCFA plaques using VH-IVUS and IVUS features. The accuracy of the hybrid feature set was obtained over 0.99 for TCFA plaque.

Keywords Clustering · Heart · TCFA · Vulnerable plaque · VH-IVUS segmentation

1 Introduction

Due to the uncertainty in medical images, developing an appropriate segmentation technique remains challenging [3, 25, 44]. Furthermore, the presence of noise caused by operators, equipment, and the environment causes considerable inaccuracies in the segmentation of medical images [14]. Intravascular Ultrasound (IVUS) imaging modality has been developed to observe the inside of coronary arteries and diagnose cardiovascular diseases [15]. This technique locates the atherosclerosis plaque and measures its distribution [15]. The Virtual Histology Intravascular Ultrasound (VH-IVUS) images contain four basic tissue

✉ Zahra Rezaei
zrezaei@iau.ac.ir

¹ Department of Computer Engineering, Marvdasht Branch, Islamic Azad University, Marvdasht, Iran

types consisting of fibro-fatty (light green), fibrotic (dark green), dense calcium (white), and necrotic core (red) [49]. Based on Nair et al. [36], the classification of plaque components is challenging due to the overlapping zones. Since the attribute data from different tissues can lie in the overlapping zone, tissue characterization and classification can be challenging [28]. For VH-IVUS imaging RGB representation, the color of a pixel is a mixture of three primary colors consist of red, green, and blue. However, pixels belonging to the border tissues are not distinguishable based on the RGB color. Since, in the VH-IVUS image, a sharp boundary of each tissue type is not discriminated, reliable segmentation of the plaque components is complex [6]. Therefore, a consistent segmentation method is needed to classify the overlapping tissue types [21]. In our previous work [45], HFCM-kNN (Hybrid FCM and kNN) was developed to precisely segment the VH-IVUS image. However, selecting the k value affects its performance. Moreover, the accuracy of the HFCM-kNN model may be degraded in the segmentation of the noisy images. In other work [43], to overcome the existing drawback, three approaches are designed and adapted. The hybrid of k-means and FCM with PSO are adapted. Moreover, hybrid approaches execute the clustering algorithm for seeding the initial swarm and group input vectors into different clusters. The cluster centroids are used as one of the particles of the swarm. The PSO algorithm is then utilized to optimize the cluster centroids. A semi-supervised model is used for pixel classification. In this study, the FCM-SNP model proposed to accurately segment the VH-IVUS image quickly. The VH-IVUS image can be precisely segmented with different color densities. Experimental evidence demonstrates the superiority of the proposed technique compared to the clustering methods. The geometric features were extracted from the segmented plaque components. Furthermore, a new segmentation and plaque extraction method in IVUS images uses a hybrid of snake and fuzzy clustering approaches. Using the snake algorithm, the user specified the initial points for drawing the curve. Based on this, the vessel area was separated from the other parts of the image using a semi-automatic method. It was suggested that the fuzzy clustering method be used to cluster the pixels of the vessel region to analyze the lumen, shadows, calcium, necrotic, and fibrotic regions. The lumen border was determined by selecting the cluster of lumen and shadows and performing the morphological operations. The plaque region was extracted by removing the lumen from the IVUS image. Based on the VH-IVUS and IVUS features, SVM classifies the plaque type into TCFA and Non-TCFA. The main contributions of the proposed model are listed below:

- Plaque border detection in VH-IVUS images was done using an automatic Level Set Plaque Border Detection (LSBPBD) algorithm.
- The model efficiently classifies unlabeled data in VH-IVUS images, eliminating the need for extensive training data using the FCM-SNP algorithm.
- Clustering validation was completed for all patient's data.
- The Hybrid of Snake and Fcm for Plaque Detection (HSFPD) algorithm accurately detected plaque borders in IVUS images.
- Geometric features were extracted from VH-IVUS and IVUS images.
- Plaque-type classification was accomplished using a fusion of VH-IVUS and IVUS features.

Other parts of this article are designed into 4 Sections. Section 2 summarizes the related works. Section 3 describes the proposed plaque border detection, segmentation, feature extraction, and plaque type classifications. Results of the proposed approach for ten patients and discussions are presented in Section 4. Finally, a discussion and conclusion are given in Section 5.

2 Related work

Several algorithms have been proposed for the segmentation of medical images using supervised and unsupervised methods [47]. Meurie et al. presented a strategy for cytological image segmentation based on the supervised pixel classification approaches, including Bayes, kNN, and SVM. Dong and Xie [12] proposed a color image segmentation scheme by hybridization of self-organizing maps (SOM) and simulated annealing (SA). The SOM algorithm projected image colors, then, the SA algorithm searched for the optimal clusters provided by prototypes. Sankari and Chandrasekar [47] proposed a semi-supervised algorithm for the segmentation of color images by applying the fast genetic algorithm and EM clustering. Wang et al. [54] presented a pixel-wise SVM classification to segment the color image. Local homogeneity pattern and Gabor filter extracted the pixel-level information and texture features. The test image is then classified by applying the SVM map. Tlig et al. [53] proposed an unsupervised image segmentation approach. They used a new texture descriptor provided by integrating Gabor filters and local binary pattern (LBP) to represent all image pixels. A fuzzy type 2 is then extended as a clustering algorithm. Aliabadian [4] suggested a robust hybrid algorithm using kNN and FCM. First, cluster centers were initialized using the kNN approach. The FCM algorithm was then applied to optimize the clustering results. Wang et al. [55] presented an improved FCM algorithm for the segmentation of noisy brain images by modifying the objective function. Jamshidi and Pilevar [19] proposed a combination of genetic algorithm and FCM for detecting several segments in brain images. Tan et al. [51, 52] used a hybrid histogram thresholding technique and FCM algorithm for splitting and merging the segments of the color image. In [39], different classification approaches were employed to integrate the ultrasound features and estimate the probability maps for pixel-wise classification using B-mode ultrasound images. The authors [34] investigated and compared some selected B-mode-based segmentation applications. Integration of RF data with higher frequency probes was discussed using more extensive B-mode data.

3 Proposed methodology

The research methodology includes pre-processing, VH-IVUS border detection, and VH-IVUS segmentation. Then, the strength of the adapted methods is investigated using cluster validity. A new algorithm for IVUS segmentation is also presented. Finally, the classification accuracy is checked using an SVM classifier. The block diagram of the proposed method is presented in Fig. 1.

3.1 Level set-based plaque border detection (LSBPBD) algorithm

LSPBD algorithm is proposed to identify the plaque border in VH-IVUS images automatically. The primary step of the Level Set (LS) method is to create the initial points to draw the initial contour. The pre-processed image is converted into the binary image I_b . The vessel region called I_{vessel} can be obtained by filling the hole in I_b . The lumen region (I_L) is computed by subtracting the I_{vessel} from I_b . After removing the small object in I_L , the lumen is the most significant area. The smallest bounding box, namely BBx, is drawn and considered for the initial counter of LS [57]. Let surface φ represent

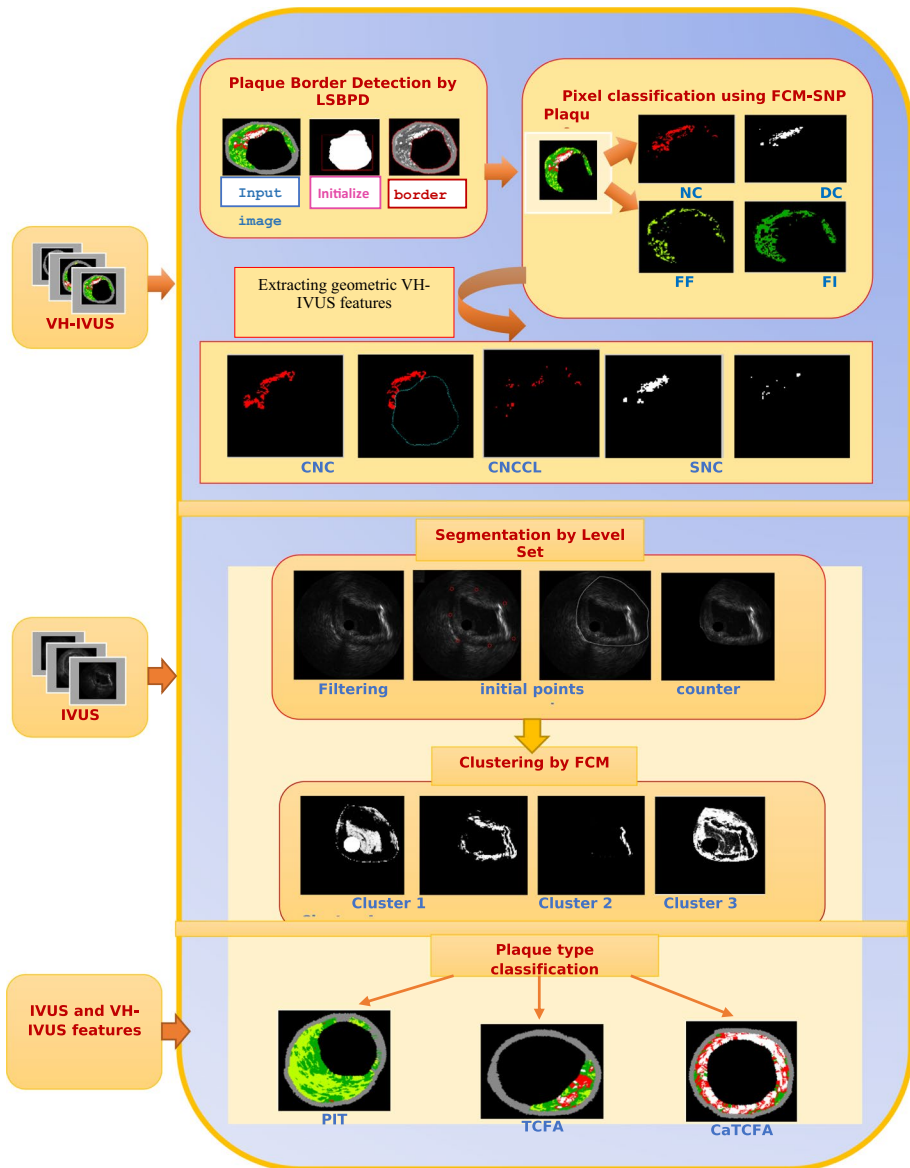


Fig. 1 Block diagram of proposed method

the inside of BBx , where $\varphi(i, j) = -1$, $i = x_1, \dots, x_1 + x_2$ and $j = y_1, \dots, y_1 + y_2$. However, the values outside the BBx are positive. To enclose the curve within the surface, φ is adjusted iteratively until convergence [40]. In the VH-IVUS image, two borders should be detected by considering the closed lumen. Therefore, counter-initialization is very important. Figure 2 displays the lumen area and initial counter. The LS method is iteratively adjusted to draw the optimized curve. Figure 3 illustrates the result of the LSPBD algorithm with different iterations, and Fig. 4 displays the plaque border detection

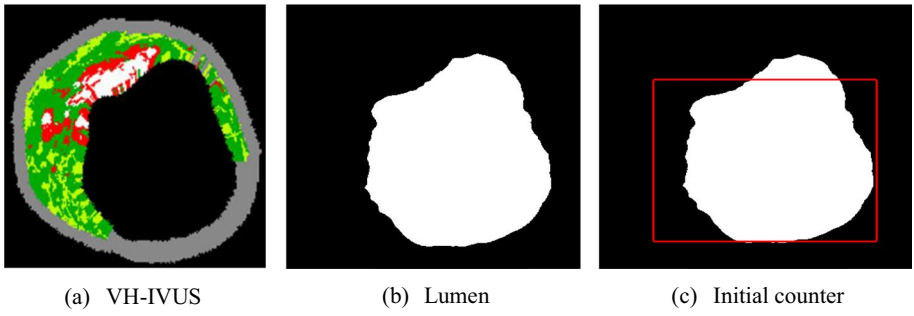


Fig. 2 Initial counter detection (a)VH-IVUS (b)Lumen (c)Initial counter

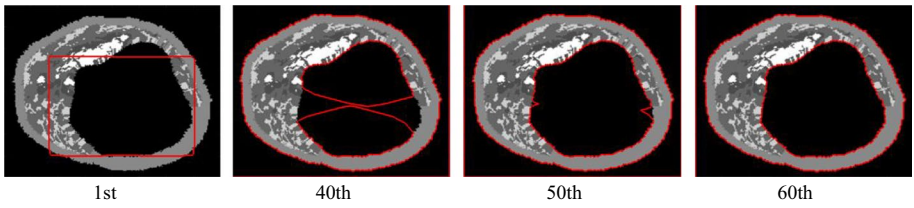


Fig. 3 Different iterations of LSPBD algorithm

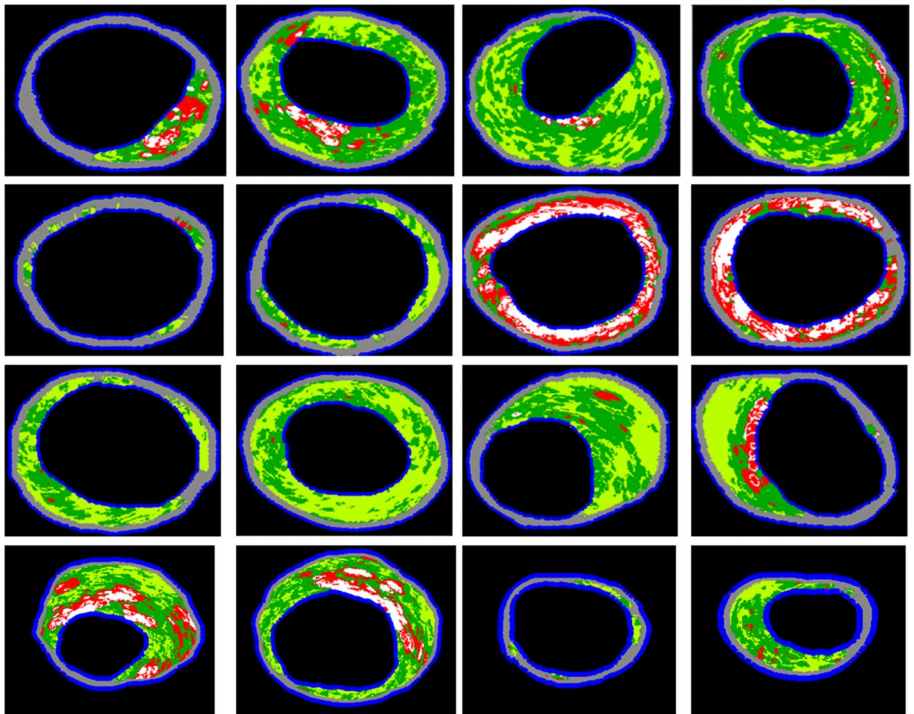


Fig. 4 Plaque border detection by LSPDB algorithm

result. The detected plaque is called I_{PA} . Moreover, the pixels belonging to the internal counter are considered the lumen border (LB).

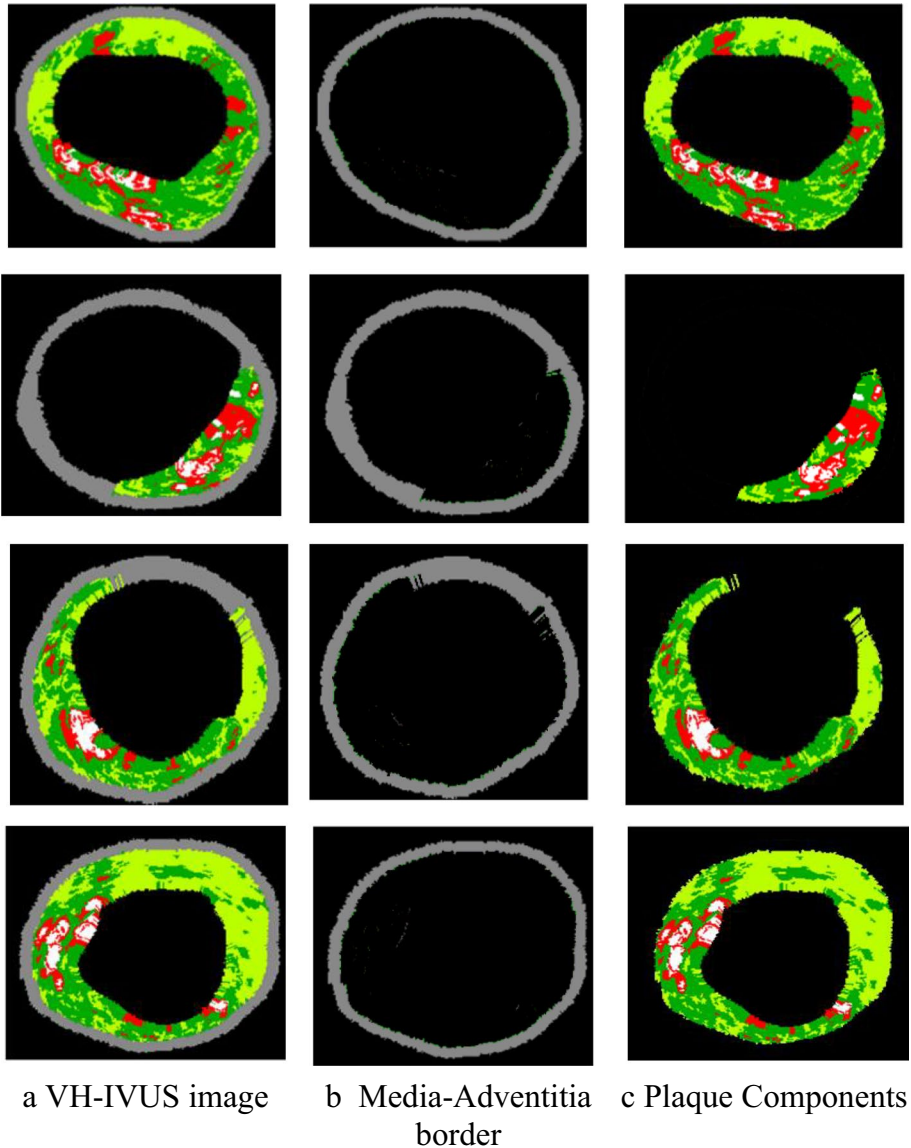


Fig. 5 Media-Adventitia removal. **a.** VH-IVUS image **b.** Media-Adventitia border **c.** Plaque Components

3.2 VH-IVUS image segmentation

3.2.1 Media-Adventitia border removing

VH-IVUS image denotes $M \times N \times 3$ matrix of RGB colors [35]. Since four plaque components are essential for the diagnosis of TCFA plaque, the Media-Adventitia border is removed using the thresholding value (See Fig. 5) [33].

3.2.2 Segmentation using clustering algorithm

The plaque components in the VH-IVUS image have overlapped borders, and to discriminate these pixels, a segmentation method should be applied that accurately separates each plaque component, including FI, FF, NC, and DC. Since, in the VH-IVUS image, a sharp boundary of each tissue type is not discriminated, reliable segmentation of the plaque components is difficult [6]. Therefore, developing a consistent segmentation method is needed to classify the overlapping tissue types [21]. A pixel-based classification method should be employed to use each pixel's information for segmentation. The clustering algorithm can divide the input data into different classes using the distance between the pixel and the center of each cluster in an unsupervised way. Therefore, clustering algorithms were used in this paper to segment the plaque components.

Many clustering techniques have been explored comprising the crisp and fuzzy scheme [57]. Three clustering algorithms, including K-means, FCM, and SOM, are adapted to segment the VH-IVUS images. VH-IVUS image of size $M \times N \times 3$ is preprocessed and reformed into the vertical three-dimensional vector $X_{RGB} = \{x_1, x_2, \dots, x_n\}$, where $n = M \times N$ and $x_{RGB} = (f_R, f_G, f_B)$ containing the RGB colors of each pixel [51, 52]. The k cluster centers as $v = \{v_1, \dots, v_k\}$ are randomly initialized for K-means and FCM algorithms [11, 20]. SOM neural network randomly initializes the weights of nodes. During the iterative learning process, a similarity criterion is utilized to find the winner node c , whose weights would be nearer to the input sample x . After the training step, data points are fed to the trained map to recognize the node with the maximal output. These nodes can be considered as the cluster center $V = \{v_1, \dots, v_m\}$ [10]. Based on the experiments, defining the cluster number for FCM and K-means is challenging. Furthermore, the SOM algorithm has to determine the number of clusters in the segmentation step. Nevertheless, some plaque components in VH-IVUS images can be absent. Therefore, accurate determination of the most appropriate k value is problematic. Clustering algorithms are greatly dependent on the initial cluster centers [27]. These algorithms may reach the local optima and miss the global optima. Furthermore, the FCM algorithm may produce a blank cluster and fail in the presence of a noisy image [48]. Qualitative assessments are conducted visually to measure the

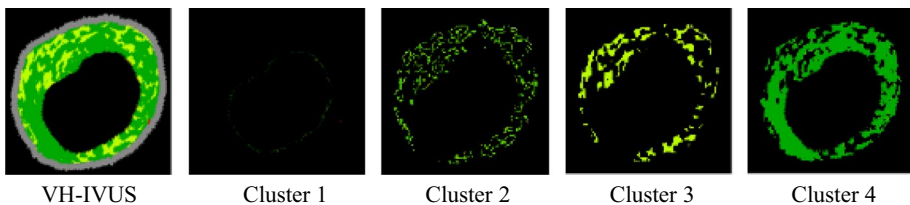


Fig. 6 Result of VH-IVUS segmentation by K-means algorithm

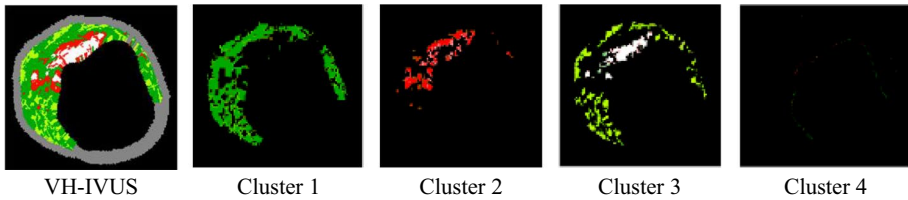


Fig. 7 Result of VH-IVUS segmentation by FCM algorithm with $k=4$

correctness of the segmentation results and investigate the strength of the FCM, K-means, and SOM algorithms. Figure 6 illustrates the inaccurate result of the K-means algorithm with $k=4$. In this figure, the VH-IVUS image has two plaque components dark green and light green. So, the clustering algorithm generates two different clusters for FI.

Based on the experimental result, the FCM algorithm considers the image's background as one cluster. Figure 7 depicts the result of FCM, while k is initialized with 4. Based on this figure, the FCM algorithm combines two colors (light green and white) in one cluster. Moreover, a redundant cluster is generated for the background.

Figure 8 illustrates VH-IVUS segmentation by FCM with $k=5$. Although FCM doesn't merge the clusters, a redundant cluster is generated for the background.

It is usually assumed that the data samples are uniformly distributed in various classes. Therefore, the learning algorithms might ignore the minority classes [26]. Therefore, clustering algorithms may combine two clusters due to the low-density cluster. Figure 9 illustrates the result of VH-IVUS segmentation using the SOM. This figure shows that light green and white pixels are merged in one cluster.

It is found that the SOM algorithm is unable to segment some of the VH-IVUS images [41]. Accurate results can be obtained with a high number of iterations, which is a rather time-consuming procedure. Qualitative assessments reveal that applying a clustering algorithm may not be sufficient for the segmentation of overlapping tissues in the VH-IVUS image. Although applying FCM and k-means have shown higher accuracy than SOM, some misclassifications have been observed.

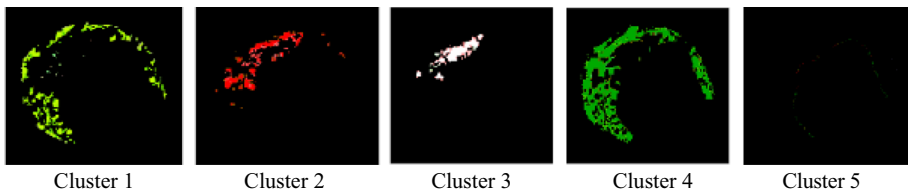


Fig. 8 Result of VH-IVUS segmentation by FCM algorithm with $k=5$

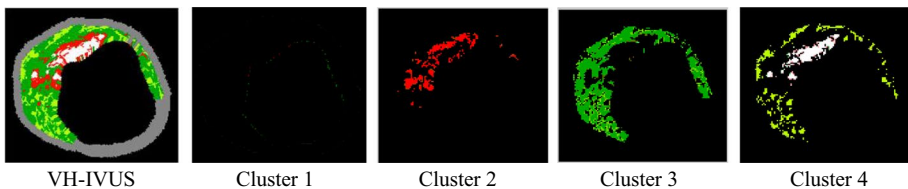


Fig. 9 Result of VH-IVUS segmentation by SOM algorithm

3.2.3 Segmentation using KMPSO and FCMP SO algorithms

PSO can reach the global optimum, so it is a very influential method for image segmentation [23]. The KMPSO model executes the k-means algorithm to generate the initial swarm. The generated cluster centroids are considered one of the particles, while other particles are adjusted randomly. In the next step, PSO is utilized to optimize the cluster centers. Moreover, the FCMP SO model is designed by hybridization of the FCM and PSO in the same manner [43]. However, the problem of merging low-density clusters still exists. Furthermore, these models must set the exact number of tissue classes in VH-IVUS images. The execution time is also high due to the application of the PSO algorithm. Figure 10 displays the results of segmentation using KMPSO. As shown in this figure, KMPSO results in weak segmentation.

3.2.4 Segmentation using FCM-SNP

To address the limitations of VH-IVUS segmentation, semi-supervised models are adapted to apply supervised learning in the classification phase. The combination of FCM clustering with supervised models proved to be more efficient in the segmentation of overlapped regions of the plaque components [45]. The proposed models involve two main phases: feature extraction and pixel-wise classification. In the first phase, the FCM algorithm is utilized for pixel clustering. Color-based features are extracted from NC, DC, FF, and FI clusters. In the second phase, pixel classification is performed by kNN, SVM, and SNP. FCM-kNN, FCM-SVM, and FCM-SNP models are designed.

Color-based feature extraction According to Bezdek et al. [8], FCM iteratively attempts to categorize similar data points $X = \{x_1, x_2, \dots, x_n\}$ with n elements into k different fuzzy clusters. In FCM, all data points have a degree belonging to the different clusters [24]. The membership matrix $(U)_{k \times n} = [u_{ij}]$ is initialized randomly to achieve fuzzy partitioning [7]. This fuzzy clustering method minimizes the objective function J by the following equation:

$$J = \sum_{j=1}^n \sum_{i=1}^k \mu_{ij}^m d^2(x_j, v_i) \quad (1)$$

n and k show the number of data points and clusters, respectively. u_{ij} is the membership value, m represents the degree of fuzziness. Parameter $d(x_j, v_i)$ calculates the distance of element x_j and cluster center v_i . The limitation of parameter u_{ij} can be defined by the following equation:

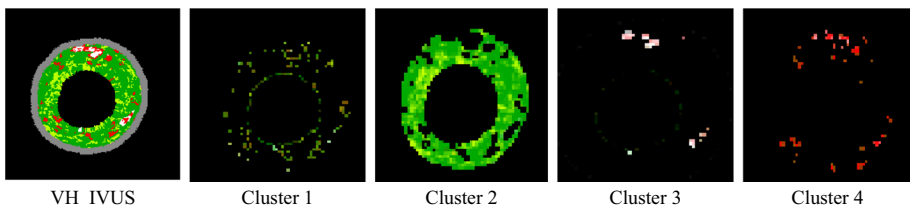


Fig. 10 The results of segmentation using KMPSO

$$\sum_{i=1}^k (\mu_{ij}) = 1, \forall j \in [1, n], \forall i \in [1, k], \mu_{ij} \in [0, 1] \quad (2)$$

The membership values μ_{ij} for representation of the membership degree of x_j in the i_{th} cluster is updated as follows:

$$\mu_{ij}^{(t)} = \frac{1}{\sum_{l=1}^k \left(\frac{d(x_j, v_l^{(t-1)})}{d(x_j, v_i^{(t-1)})} \right)^{2/(m-1)}} \quad (3)$$

where, t shows the iteration number, and $d(x_j, v_i)$ is the Euclidian distance of v_i and x_j [24]. Additionally, the center of each cluster v is updated by mean of weighted data points based on the following equation:

$$v_i^{(t)} = \frac{\sum_{j=1}^n (\mu_{ij}^{(t)})^m x_j}{\sum_{j=1}^n (\mu_{ij}^{(t)})^m} \quad (4)$$

The process will be stopped when the improvement between two consecutive iterations ($t-1$ and t) is less than error \mathcal{E} .

$$\|v_i^{(t)} - v_i^{(t-1)}\| < \varepsilon \quad (5)$$

FCM algorithm divides the background and foreground, whereas the plaque component is related to the region of interest, and the background is the remainder of the image. Since the VH-IVUS image has four different colors, cluster number k is initially set to 5 (one cluster represents the background, and others illustrate the NC, DC, FF, and FI). After the convergence of FCM clustering, the intensities are redistributed to the different clusters [30]. The cluster index and CI vector created ranged from 1 to k . The CI reshaped to the matrix, namely CIM . Cluster labeling is performed using the mean values of R , G , and B for each cluster center [12]. The variable $m < k$ controls the label of each cluster. The outliers are removed from the NC and DC images. Non-zero pixels of NC, DC, FF, and FI clusters copied to the color-based feature matrix $CFM = \{cf_1, cf_2, \dots, cf_z\}$ and their corresponding labels saved into the $Label$ vector, where $Label(cf_i)$ determines the class of cf_i and z shows the number of features in CFM . These features are used as training sets to build a predictive model. Algorithm 1 shows the pseudocode of the color-based feature extraction method. The main sections of Algorithm 1 were considered for calculating the complexity. The complexity of FCM algorithm is $O(ndk^2i)$, where n is number of data points, d shows number of dimensions, k is number of clusters, and I represent the number of iterations. There are two loops with $O(kMN)$ and $O(CMN)$ order, respectively, where $c = k-1$.

Algorithm 1 Pseudo-code of color-based feature extraction

```

1: Input: VH-IVUS image of size  $M \times N$ 
2: Set  $k \leftarrow 5$ ,  $n \leftarrow M \times N$ 
3: Removing Media-Adventitia from VH-IVUS image to generate the VH
   image
4: //Applying FCM and generate cluster index  $CI$ 
5:  $CI \leftarrow FCM(VH, k)$ 
6: Convert  $CI$  vector into a matrix namely  $CIM$ 
7: //Assigning each pixel of VH image to cluster 1 to  $k$  using  $CIM$ 
8:  $m \leftarrow 1$ //Cluster number
9: // Cluster labeling
10: While ( $m < k$ ) do
11:   for  $i \leftarrow 1$  to  $M$  do
12:     for  $j \leftarrow 1$  to  $N$  do
13:       if  $CIM[i, j] == m$  then
14:          $Cluster_m[i, j] \leftarrow VH[i, j]$ //Copy pixel intensity to  $cluster_m$ 
15:       end if
16:     end for
17:   end for
18:    $m \leftarrow m + 1$ 
19: end while
20: Assign  $Cluster_1, \dots, Cluster_k$  to  $NC, DC, FF, FI$ , and background
21: Outlier removal form  $NC$  and  $DC$ 
22: // Extracting color features  $CFM$  and their labels
23: Set  $PlaqueComponent = \{NC, DC, FF, FI\}$ 
24: Set  $m \leftarrow 1$ ,  $c = k - 1$ ,  $row = 1$ 
25: While ( $m \leq c$ ) do
26:   for  $i \leftarrow 1$  to  $M$  do
27:     for  $j \leftarrow 1$  to  $N$  do
28:       if  $PlaqueComponent_m[i, j] > 0$  then
29:         //Copy the intensity value of pixel  $i, j$  to  $CFM$ 
30:          $CFM[row] \leftarrow PlaqueComponent_m[i, j]$ 
31:          $Label[row] \leftarrow m$ 
32:          $row \leftarrow row + 1$ 
33:       end if
34:     end for
35:   end for
36:    $m \leftarrow m + 1$ 
37: end while
38:  $z \leftarrow row - 1$ 
39: Output: Color feature matrix( $CFM$ ),  $Label$ ,  $z$ 

```

Pixel wise classification using SNP algorithm The SNP method is proposed to classify the testing image by means of minimum Euclidian distance. The testing image of size $M \times N$ is preprocessed, and the feature vector $XT = \{x_1, \dots, x_n\}$ is created, where $n = M \times N$. For all pixels belonging to the XT , the minimum distance between x_i and CFM is computed. The lowest value of the minimum distances is selected and its corresponding value in $Label$ vector considers as its class. The label of each pixel is set based on their class such that $NC = 1$, $DC = 2$, $FF = 3$, and $FI = 4$. For segmentation of test image, four different images including NC_T, DC_T, FF_T, FI_T are created based on the label of each pixel. Algorithm 2 shows the pseudo-code for the proposed pixel-wise classification using the SNP algorithm. In Algorithm 2, the complexity of calculating the minimum Euclidian distance of x_i and CFM is $O(nz)$, where $n = M \times N$ and z is the number of color features in CFM . The complexity of segmentation part is $O(MN)$.

Algorithm 2 Pseudo-code for segmentation using the SNP algorithm

```

1: Input: Testing VH-IVUS image of size  $M \times N$ ,  $CFM = \{cf_1, cf_2, \dots, cf_z\}$ 
2: Removing Media-Adventitia from VH-IVUS image to generate  $VH_T$  image
3: converting  $VH_T$  image to a vector  $XT = \{x_1, \dots, x_n\}$ 
4: Set row←1
5: for i←1 to n do
6:   for j←1 to z do
7:     //Calculating the Euclidian distance( $Ed$ ) of  $x_i$  and  $CFM$ 
8:      $ED[row]=Ed(x(i), CFM(j))$ 
9:     row ← row +1
10:   end for
11: end for
12:  $Min \leftarrow \text{minimum}(ED)$ 
13:  $IndexL = \text{find}(\text{corresponding value of } Min \text{ index in Label vector})$ 
14:  $CLT(x(i)) \leftarrow IndexL$ 
15: end for
16: converting  $CLT$  to the matrix with size of  $M \times N$ 
17: //Segmentation of  $VH_T$ 
18: Create four empty images ( $NC_T, DC_T, FF_T, FT_T$ ) of size  $M \times N$ 
19: for i←1 to M do
20:   for j← 1 to N do
21:     if  $CLT[i, j]=1$  then  $NC_T[i, j]=255$ 
22:     else if  $CLT[i, j]=2$  then  $DC_T[i, j]=255$ 
23:     else if  $CLT[i, j]=3$  then  $FF_T[i, j]=255$ 
24:     else  $FI_T[i, j]=255$ 
25:   end if
26: end for
27: end for
28: Output:  $NC_T, DC_T, FF_T, FT_T$  images

```

3.3 Validation of segmentation

The 599 Grayscale IVUS and VH-IVUS images were taken from 10 patients used. The size of VH-IVUS was 400×400 in RGB format, which was provided by a 20 MHz ultrasonic device [50]. The capacity of clustering algorithms is represented by the silhouette validity index [17]. The silhouette accuracy $s(i)$ of the object i is achieved by the following equation:

$$s(i) = b(i) - a(i) / \max\{a(i), b(i)\} \quad (6)$$

where $a(i)$ depicts the average distance between the i th data and rest data points in the cluster, and $b(i)$ represents the lowest average distance between them. This index illustrates the range of -1 to $+1$ for each pixel and determines the similarity of the pixels belonging to one cluster compared to the other clusters [5].

FCM-kNN [42], FCM-SNP, and FCM-SVM models are implemented in Matlab software. The Statistics Toolbox is used for kNN and K-means algorithms, while the Fuzzy Logic Toolbox is utilized for the FCM algorithm. Multi-class SVM is also employed for pixel classification using LIBSVM [9]. The capacity of pixel-wise classification is represented with a silhouette index [17]. This method measures cluster validity to investigate the power of the proposed approaches for classifying overlapped tissues. Figure 11 depicts the results of SW by applying FCM-kNN, FCM-SNP, and FCM-SVM algorithms for patients 1 to 10. Based on this figure, the SW for FCM-SVM for Patient 1 shows the higher

result, however, for other patients FCM-SNP achieved the best SW result that shows this method accurately segment the VH-IVUS images.

Figure 12 shows the clustering accuracy for patients 1 to 10 by applying FCM-kNN, FCM-SNP, and FCM-SVM models. As shown in this figure, FCM-SVM achieves the best result of 0.97 for patient 1, while FCM-SNP obtains the best results for the other patients. The results of FCM-SVM and FCM-SNP are similar for patient 8. FCM-SVM presents the worst result of 0.65 for patient 2. For Patients 1, 3, 4, 5, 6, 7, 8, 9, and 10, FCM-kNN achieves the worst results.

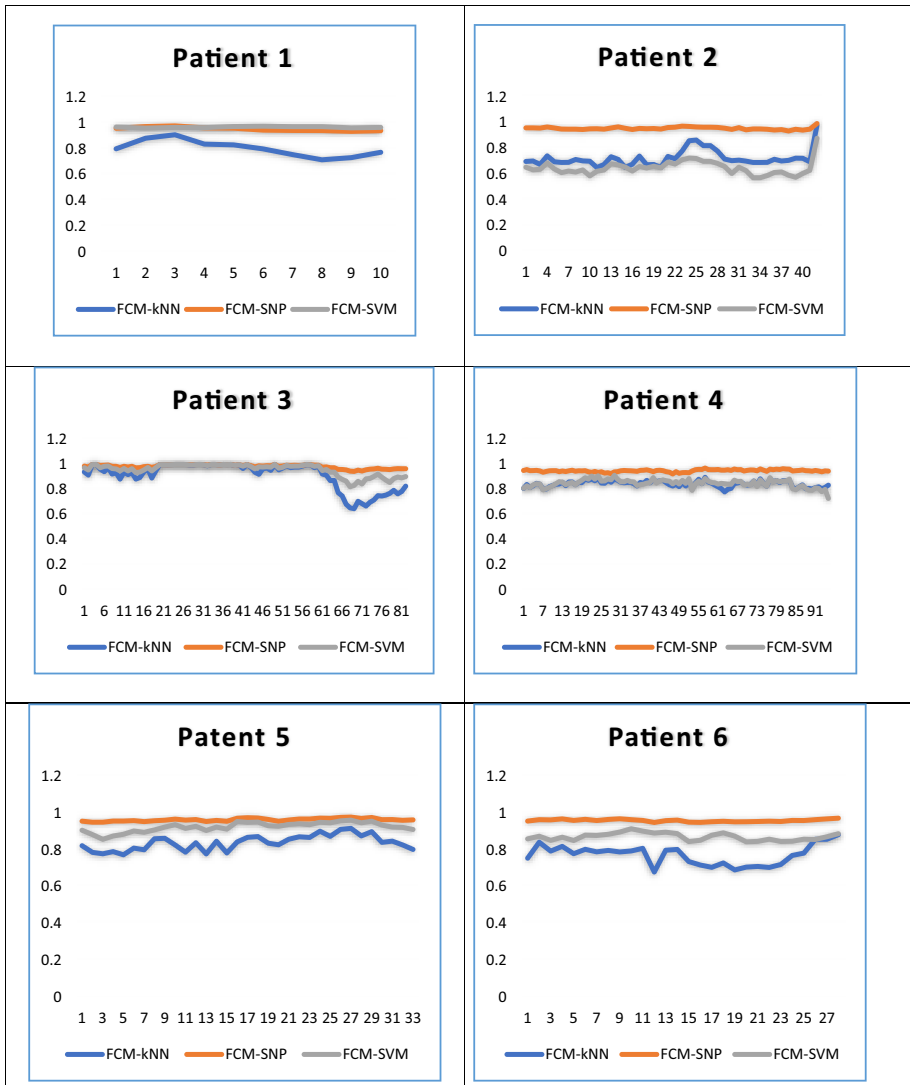


Fig. 11 Results of SW by applying FCM-kNN, FCM- SNP, and FCM-SVM algorithms

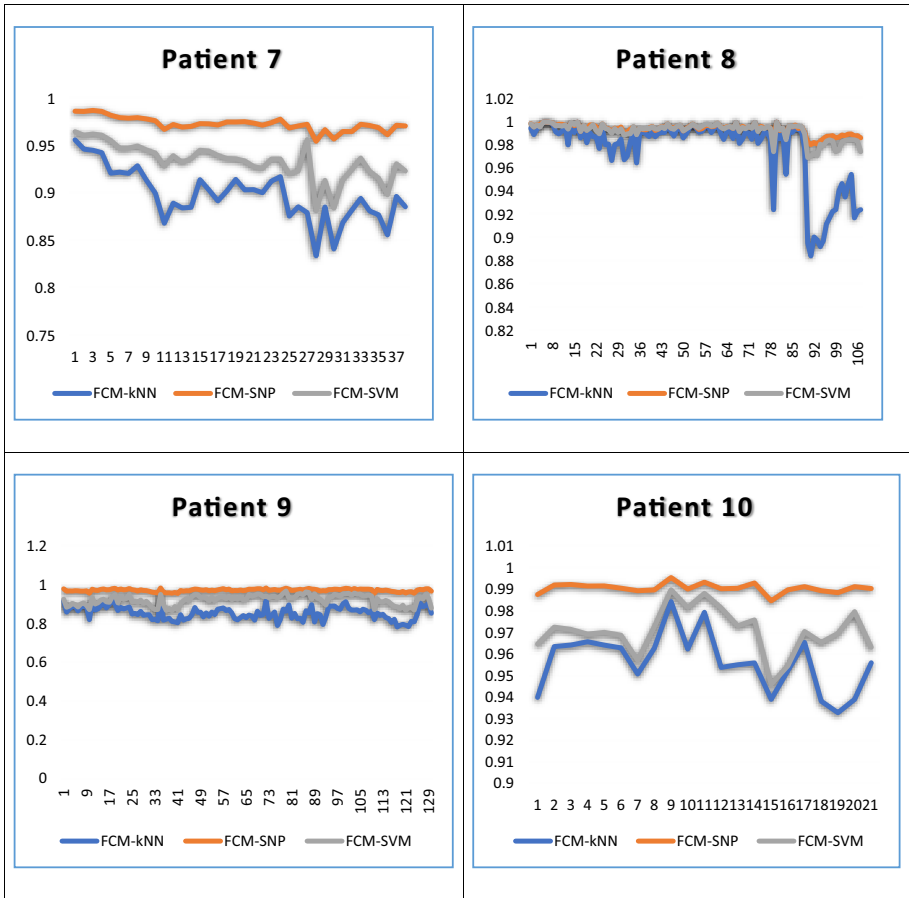


Fig. 11 (continued)

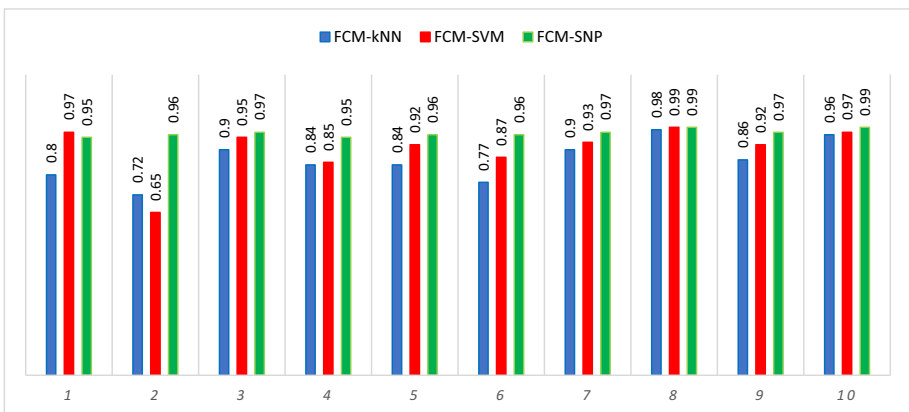


Fig. 12 Comparison between average clustering accuracy for patients 1 to 10 when applying FCM-kNN, FCM-SNP, and FCM-SVM algorithms

Tables 1, 2, and 3 illustrate the segmentation results for different types of VH-IVUS images by applying the FCM-SNP model. The silhouette validity index is computed for each cluster, and the average is depicted as SW (Silhouette Weight).

3.4 Feature extraction

Geometric features are extracted from the clustered images to classify the TCFA and Non-TCFA. The details of Confluent Components Detection (CCD) and NC Layers Detection (NCLD) algorithms are presented here. Moreover, the Plaque Area (PA), Vessel Area(VA), Lumen Area (LA), and Plaque Burden (PB) are calculated [45].

3.4.1 Confluent components detection (CCD) algorithm

The thresholding method is used to binarize the NC image [31]. The connected component labeling (CCL) algorithm segments the binary image and detects the confluent NC (CNC) and scattered NC (SNC) [46]. In the same way, confluent DC (CDC) and microcalcification (MicroCa) were detected. We need to identify the pixels that are common to both CNC and lumen border to detect CNC in contact with the lumen (CNCCL). The following is a step-by-step description of the process for implementing the CCD algorithm [45]:

Table 1 Results of FCM-SNP (VH-IVUS with four plaque components)

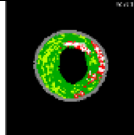
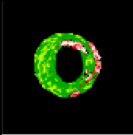
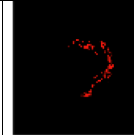
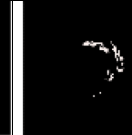
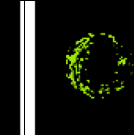
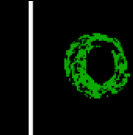
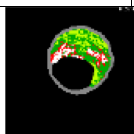
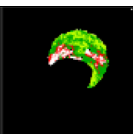
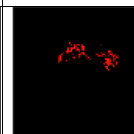


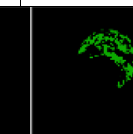
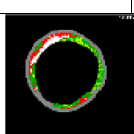
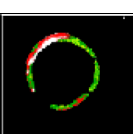
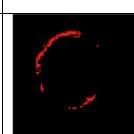
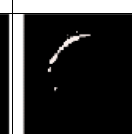
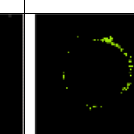
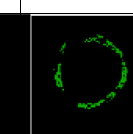
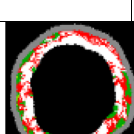

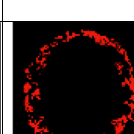

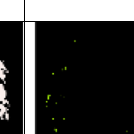
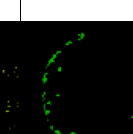
VH-IVUS	Plaque	NC	DC	FF	FI	SW
						0.97
						0.98
						0.98
						0.94

Table 2 Results of FCM-SNP (VH-IVUS with three plaque components)

VH-IVUS	Plaque	NC	FF	FI	SW
					0.99
					0.96
					0.99
					0.98

Step 1: The CCL algorithm is performed on the NC binary image to segment each NC segments [18].

Step 2: The canny edge detection algorithm extracts the edge of NC segments, and their diameters (d) are calculated.

Step 3: If the size of $d_i \geq 14$ pixels, the NC_i segment is classified as CNC_i ; otherwise, it is called SNC .

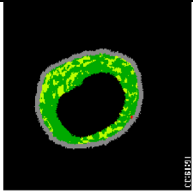
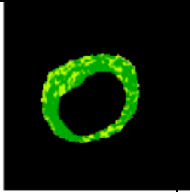
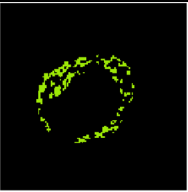
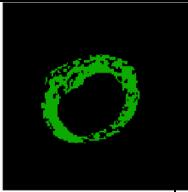
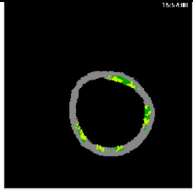
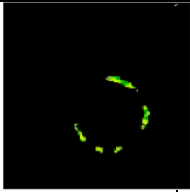
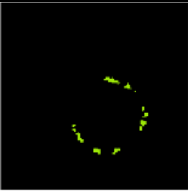
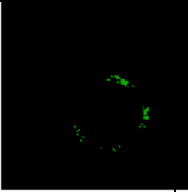
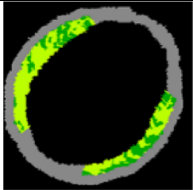
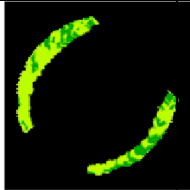
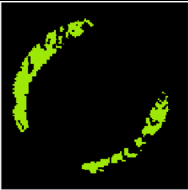
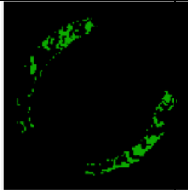
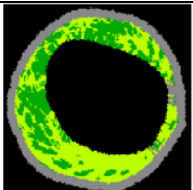
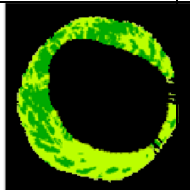
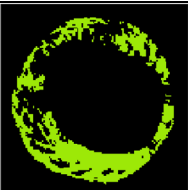
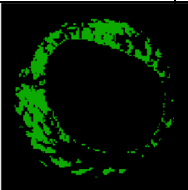
Step 4: C_i is a 2D matrix that stores the coordinates of CNC_i . The possible shared points between CNC_i and the lumen border are found to create the $CNCCL$ segments.

3.4.2 NC layers detection (NCLD) algorithm

NCLD algorithm proposes to detect the number of NC layers in VH-IVUS images. Drawn lines from the center of the image are used to identify the pixels that intersect with the CNC segments. If a single segment shares pixels with one of the drawn lines, then it can be inferred that the NC pertains to a single layer. The final count of NC layers is computed and denoted as NCL . In the same way, DCL stores the determined DC layers. The process of calculating the NC layers involves repeating steps 1 to 4 for a total of m times [45].

Step 1: The binary image, CNC , is created by combining multiple images identified as CNC_1 , CNC_2 , and so on up to CNC_m .

Table 3 Results of FCM-SNP (VH-IVUS with two plaque components)

VH-IVUS	Plaque	FF	FI	SW
				0.98
				0.99
				0.98
				0.96

- Step 2: Radial lines are drawn from the center of the CNC image. The representation of all pixels belonging to each line is done using Bresenham’s line algorithm [56].
- Step 3: The lines are examined to identify the shared pixels with CNC_i , which indicates that this line passes through this segment.
- Step 4: The number of crossing points of lines and CNC segments stored in the VH_{NCL} feature to show the number of NC layers.

Figure 13 illustrates the results of NC , CNC , $CNCCL$, SNC , DC , CDC , and $MicroCa$ obtained by the proposed geometric feature extraction algorithm. These plaque component features were used for classification.

3.5 Hybrid of snack and FCM for plaque detection (HSFPD) using IVUS image

The Volcanic platform provides IVUS features, including Lumen Area (LA), Media Area (MA), Lipid Core Area (LCA), Fibrous Area (FA), Fibro Lipidic Area (FLA), and Calcified

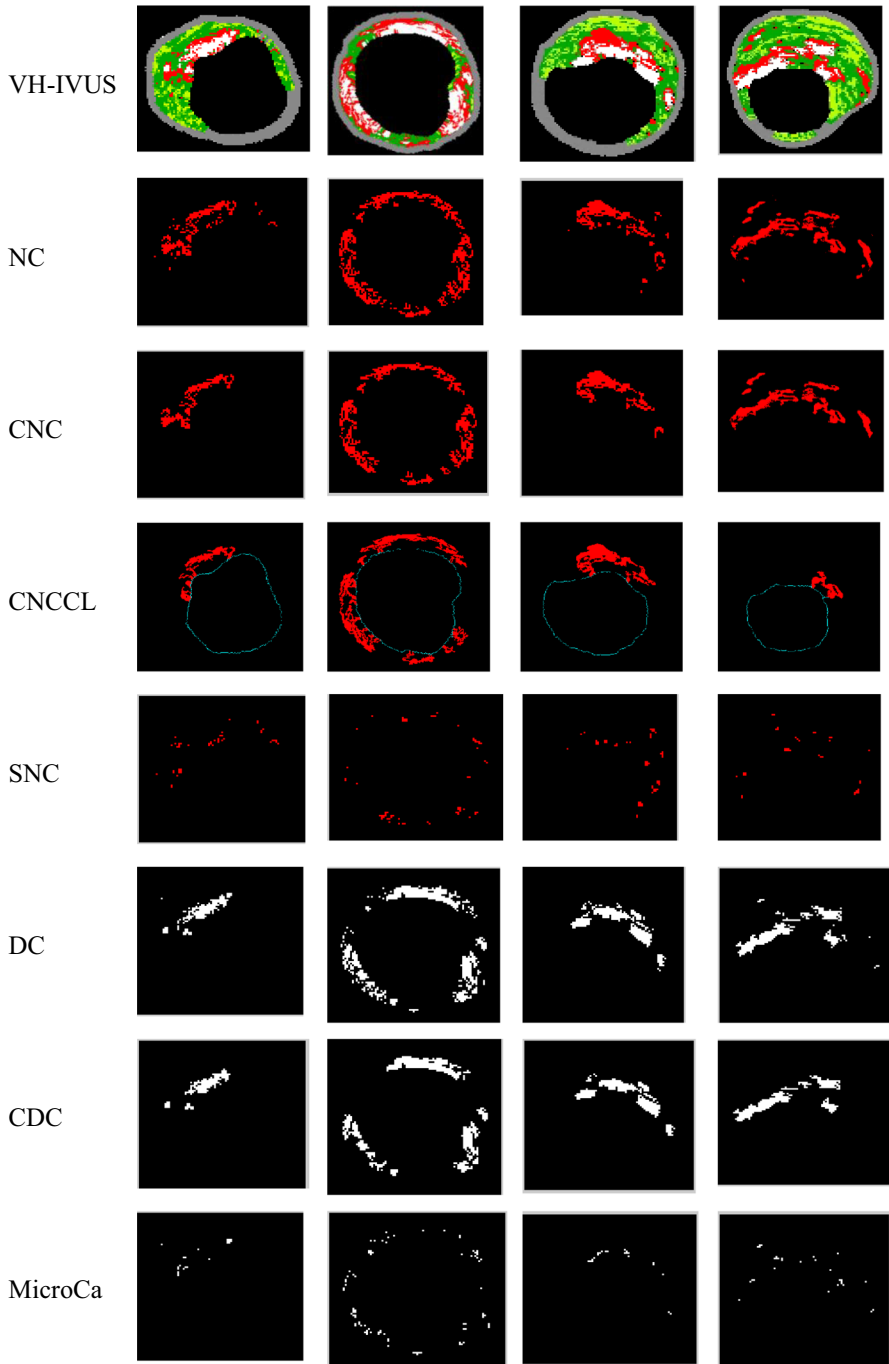


Fig. 13 Plaque component features

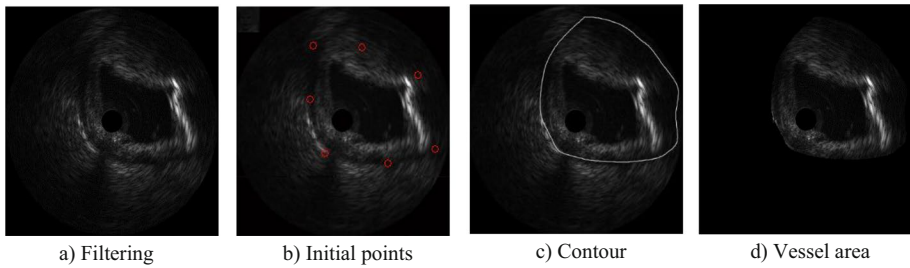


Fig. 14 Segmentation of the vessel area in IVUS image (a) Filtering (b) Initial points (c) Contour (d) Vessel area

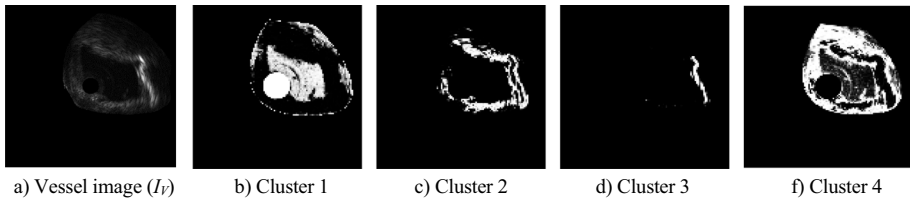


Fig. 15 Clustering of vessel image (a) Vessel image (I_V) (b) Cluster 1 (c) Cluster 2 (d) Cluster 3 (e) Cluster 4

Area (CA). The Maximum Vessel Diameter (MaVD), Minimum Vessel Diameter (MiVD), Average Vessel Diameter (AVD), Maximum Lumen Diameter (MaLD), Minimum Lumen Diameter (MiLD), and Average Lumen Diameter (ALD) are measured as well [37, 38]. However, in case of unavailable IVUS features, segmentation and plaque detection must be performed using IVUS images. In this section, a new method for segmentation and plaque border detection in IVUS images [22] is presented using a hybrid of snake and FCM.

3.5.1 Snake-based segmentation

Due to the noise in IVUS, the image was smoothed using a Gaussian filter with a sigma length of [13, 14]. The user specified initial points in the plaque area of the IVUS image. Based on the initial points, the snake algorithm drew a contour, and the vessel area was separated from other parts of the image. The resulting image was named I_V . Figure 14 shows the segmentation of the vessel region in the IVUS image using the snake algorithm. The red points in Fig. 14b, illustrates the user's selected area.

3.5.2 Clustering by FCM

The FCM algorithm is used to cluster the vessel image. As a result, four clusters containing the plaque components were obtained. Each cluster has a center to represent all pixels belonging to that cluster. The next stage determined which clusters belong to the lumen and shadow areas in the vessel image. Based on the experiments, the cluster with minimum center value includes areas of lumen called I_L . Figure 15 shows the images obtained from

FCM clustering. As shown in this figure, four clusters were generated by the FCM algorithm. Their centers were checked to select the lumen area.

3.5.3 Extraction of plaque area in vessel image

The plaque image I_p was extracted by removing the I_L from the I_v . The plaque border was then drawn in the IVUS image, and this area was filled with grey color and then cropped from the original image. The border of the segmented plaque was also drawn using the standard method to compare the proposed method with the state-of-the-art. Figure 16 compares plaque border detection with the standard and proposed methods. Figure 17 shows the boundaries extracted by two methods in one image.

4 Results

4.1 Evaluation

4.1.1 Evaluation metrics

A confusion matrix is calculated to evaluate the classification result (Table 4). Each element of the matrix is as follows:

TN: Negative records correctly recognized as negative.

TP: Positive records correctly recognized their category as positive.

FP: The negatives that are mistakenly recognized as positive.

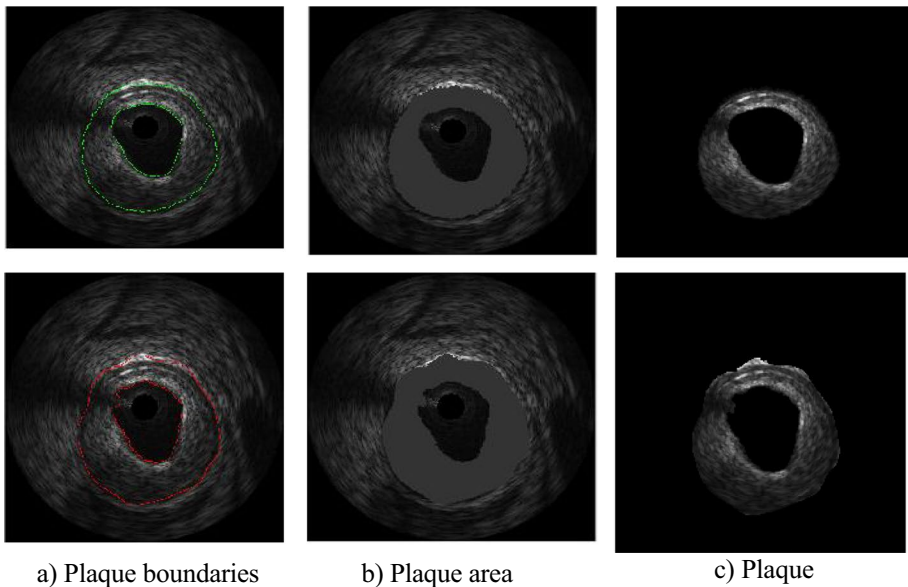


Fig. 16 Comparison of plaque border in the standard method (first row) and the proposed method in this article (second row). **a** Plaque boundaries **b** Plaque area **c** Plaque

Fig. 17 Comparison of the extracted plaque boundaries by the standard method (green lines) and the proposed method (red lines)

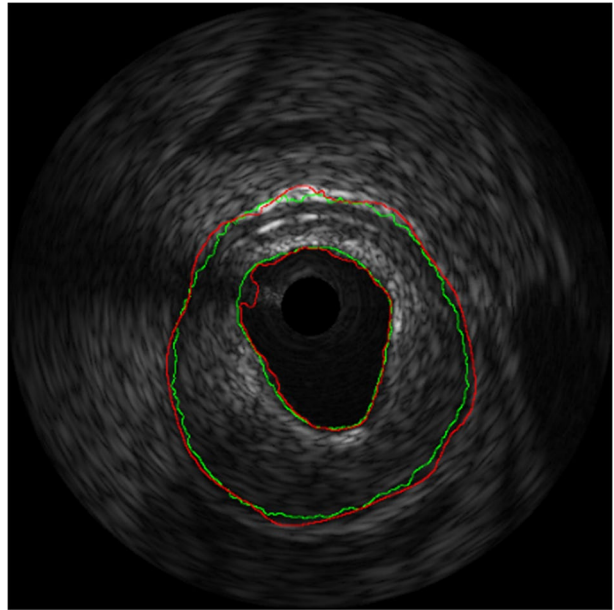


Table 4 Confusion matrix [32]

		Actual labels		Total
		1 (Positive)	0 (Negative)	
Predicted labels	1 (Positive)	TP	FP	Predicted total positives
	0 (Negative)	FN	TN	Predicted total negatives
Total		Actual total positives	Actual total negatives	

FN: The positive records were mistakenly recognized as negative.

Based on the confusion matrix, accuracy, sensitivity, specificity, precision, and F-score are selected to evaluate the proposed method [16, 57].

Accuracy identifies the percentage of test data that is correctly estimated out of the total data.

$$\text{Accuracy} = \frac{TP + TN}{TP + FN + TN + FP} \quad (7)$$

The chance of a positive test result is called sensitivity (true positive rate), based on the person being positive.

$$\text{Sensitivity} = \frac{TP}{TP + FN} \quad (8)$$

Specificity (true negative rate) denotes the likelihood of a negative test result occurring when the individual is genuinely negative.

$$\text{Specificity} = \frac{TN}{TN + FP} \quad (9)$$

Precision, also known as positive predictive value, represents the proportion of relevant instances within the retrieved cases.

$$\text{Precision} = \frac{TP}{TP + FP} \quad (10)$$

The traditional F-measure, also known as the balanced F-score, is a metric that combines precision and recall using their harmonic mean.

$$F1 = 2 \times \frac{\text{Precision} \times \text{Recall}}{\text{Precision} + \text{Recall}} \quad (11)$$

4.2 Data labeling

Histopathological classification knowledge can be used to classify plaque types. Coronary lesions are classified as TCFA, ThCFA, CaTCFA, PIT, FP, and FC plaques. Table 5 summarizes the criteria for plaque type classification. The first column shows the plaque type, the second column includes their clinical information, and the last column represents the geometric feature mapped with the second column.

To label the VH-IVUS images, the percentage of each tissue type related to the plaque area is calculated. Then, the label is provided by applying the criteria in Table 5. Table 6 illustrates the number of VH-IVUS images for each class, including PIT, FC, Fibrotic, TCFA, CaTCFA, and ThCFA. Because some plaques were unavailable in the VH-IVUS dataset images, SVM selected three significant groups for classification: PIT (439), TCFA (102), and CaTCFA (58).

4.3 Statistical analysis

The features extracted are used to create the VH-IVUS feature vector, which is denoted by $VH-IVUS = \{NC, DC, FI, FF, NCCL, CNC, CNC, CNCCL, CDC, NCL, DCL, MicroCa, SNC, PA, VA, LA, PB\}$. Geometric features are classified into PIT, TCFA, and CaTCFA according to the criteria of plaque-type classification. All geometrical features have been evaluated for their mean, standard deviation, and p-value [1, 2]. The results are presented

Table 5 Criteria of plaque type classification

Plaque type	Histopathological Criteria	Geometric feature
TCFA: Thin-Cap FibroAtheroma	<ul style="list-style-type: none"> ● Confluent DC < 10% ● Confluent NC > 10% ● Necrotic core in contact with the lumen ● Single or multiple CNC ● Plaque burden ≥ 40% 	<ul style="list-style-type: none"> ● <i>CDC</i> < 10% ● <i>CNC</i> > 10% ● <i>NCCL</i> > 0 ● <i>NCL</i> > 0 ● <i>PB</i> ≥ 40%
ThCFA: Thick-Cap FibroAtheroma	<ul style="list-style-type: none"> ● Confluent DC < 10% ● Confluent NC > 10% ● NC not adjacent to the lumen ● Plaque burden ≥ 40% 	<ul style="list-style-type: none"> ● <i>CDC</i> < 10% ● <i>CNC</i> > 10% ● <i>NCCL</i> = 0 ● <i>PB</i> ≥ 40%
CaTCFA: Calcified TCFA	<ul style="list-style-type: none"> ● Confluent DC > 10% ● Confluent NC > 10% ● NC adjacent to the lumen ● Plaque burden > 40% 	<ul style="list-style-type: none"> ● <i>CDC</i> > 10% ● <i>CNC</i> > 10% ● <i>NCCL</i> > 0 ● <i>PB</i> ≥ 40%
PIT: Pathological Intimal Thickening	<ul style="list-style-type: none"> ● Mixture of fibrous and fibro fatty ● Fibro fatty ≥ 15% ● Confluent NC < 10% ● Confluent DC < 10% ● Plaque burden ≥ 40% 	<ul style="list-style-type: none"> ● <i>FI</i> is high ● <i>FF</i> ≥ 15% ● <i>CNC</i> < 10% ● <i>CDC</i> < 10% ● <i>PB</i> ≥ 40%
FP: Fibrotic plaque	<ul style="list-style-type: none"> ● Has mainly fibrous tissue ● Fibro fatty plaque < 15% ● Confluent NC < 10% ● Confluent DC < 10% 	<ul style="list-style-type: none"> ● <i>FI</i> is high ● <i>FF</i> < 15% ● <i>CNC</i> < 10% ● <i>CDC</i> < 10%
FC: Fibro Calcified	<ul style="list-style-type: none"> ● Contain high FI ● Confluent DC > 10% ● Confluent NC < 10% 	<ul style="list-style-type: none"> ● <i>FI</i> is high ● <i>CDC</i> > 10% ● <i>CNC</i> < 10%

Table 6 Dividing VH-IVUS data set into PIT, FC, Fibrotic, TCFA, CaTCFA, and ThCFA

PIT	FC	Fibrotic	TCFA	CaTCFA	ThCFA
439	0	0	102	58	0

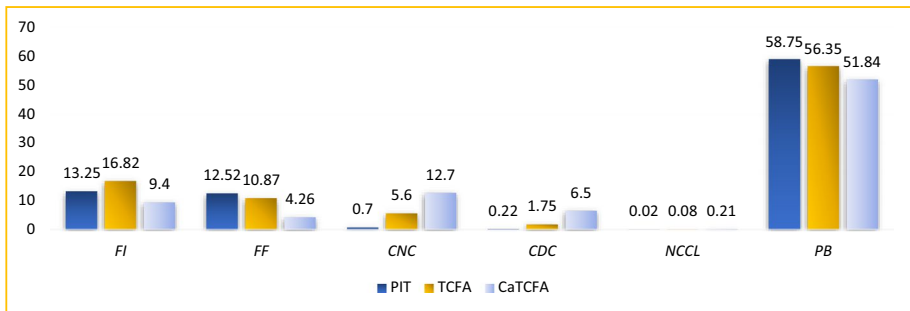
in Table 7. All the geometric features have achieved a p-value < 0.0001, which signals their ability to differentiate [1, 2]. This table shows that NC, NCCL, CNC, and CNCCL show higher values for TCFA and classes than PIT. However, FF is higher for PIT than for other classes.

Figure 18 demonstrates the mean value of the VH features for PIT, TCFA, and CaTCFA plaque. The x-axis and y-axis indicate each feature’s mean area (mm²), respectively.

According to Fig. 13, PIT attained the highest value of FF. Moreover, based on the criteria, CDC > 10% for CaTCFA plaque should be less than 10% for other types. The highest value of CDC among the different classes is observed in CaTCFA. The CNC values for TCFA and CaTCFA lesions are greater than 10%. The criteria of CaTCFA are satisfied as per the figure depicted, where CNC > 10%, CDC > 10%, NCCL > 0, and PB is greater than or equal to 40%. However, for PIT lesions, CNC is less than 10. Additionally, CNC < 10% and CDC < 10% shows for PIT plaque. The TCFA plaque indicated CNC > 10%, CDC < 10%, NCCL > 0, and PB > 40%. Moreover, the correlation heatmap for VH-IVUS features is calculated and displayed in Fig. 19. The x and y labels show the feature’s names. The 18 VH-IVUS feature was used to create the correlation between these features. The

Table 7 Mean \pm STD

Features	Mean \pm STD		
	PIT	TCFA	CaTCFA
<i>NC</i>	1.12 \pm 1.27	6.18 \pm 2.45	13.34 \pm 3.40
<i>DC</i>	0.35 \pm 0.71	2.30 \pm 1.38	7.34 \pm 1.61
<i>FI</i>	13.25 \pm 11.71	16.82 \pm 11.62	9.40 \pm 8.74
<i>FF</i>	12.52 \pm 11.00	10.87 \pm 8.71	4.26 \pm 6.68
<i>NCCL</i>	0.02 \pm 0.02	0.08 \pm 0.06	0.21 \pm 0.09
<i>DCCL</i>	0.01 \pm 0.01	0.04 \pm 0.03	0.20 \pm 0.10
<i>CNC</i>	0.77 \pm 1.04	5.60 \pm 2.34	12.70 \pm 3.43
<i>CNCCL</i>	0.27 \pm 0.62	3.72 \pm 2.69	11.36 \pm 4.83
<i>CDC</i>	0.22 \pm 0.63	1.75 \pm 1.45	6.50 \pm 1.56
<i>MicroCa</i>	0.09 \pm 0.15	0.53 \pm 0.20	0.84 \pm 0.29
<i>SNC</i>	0.35 \pm 0.33	0.57 \pm 0.28	0.64 \pm 0.20
<i>NCL</i>	0.54 \pm 0.50	1.00 \pm 0.00	1.00 \pm 0.00
<i>DCL</i>	0.22 \pm 0.42	0.95 \pm 0.23	1.00 \pm 0.00
<i>PA</i>	28.29 \pm 16.36	35.37 \pm 11.41	41.55 \pm 4.03
<i>VA</i>	49.73 \pm 27.50	64.53 \pm 21.32	80.23 \pm 3.58
<i>LA</i>	21.44 \pm 15.14	29.16 \pm 13.55	38.68 \pm 4.85
<i>PB</i>	58.75 \pm 14.71	56.35 \pm 10.73	51.84 \pm 5.31

**Fig. 18** The mean of VH-IVUS features

number of rows and columns is equal in his matrix. It provides the possibility to identify the relationships between variables. Different colors in the heatmap matrix differentiate the positive and negative correlation values. As shown in this figure, some features correlate highly to other features such as *NC* with *DC*, *NCCL*, *CNC*, *CNCCL*, and *MicroCa*. However, *NC* has a low correlation to the *FI*, *LA*, and *PB* and a negative correlation with *FF*.

4.4 Plaque type classification

SVM is an algorithm for supervised learning. It is typically employed to handle classification and regression tasks. The algorithm works by locating a hyperplane in a high-dimensional space, splitting the data points into different classes. SVM has different

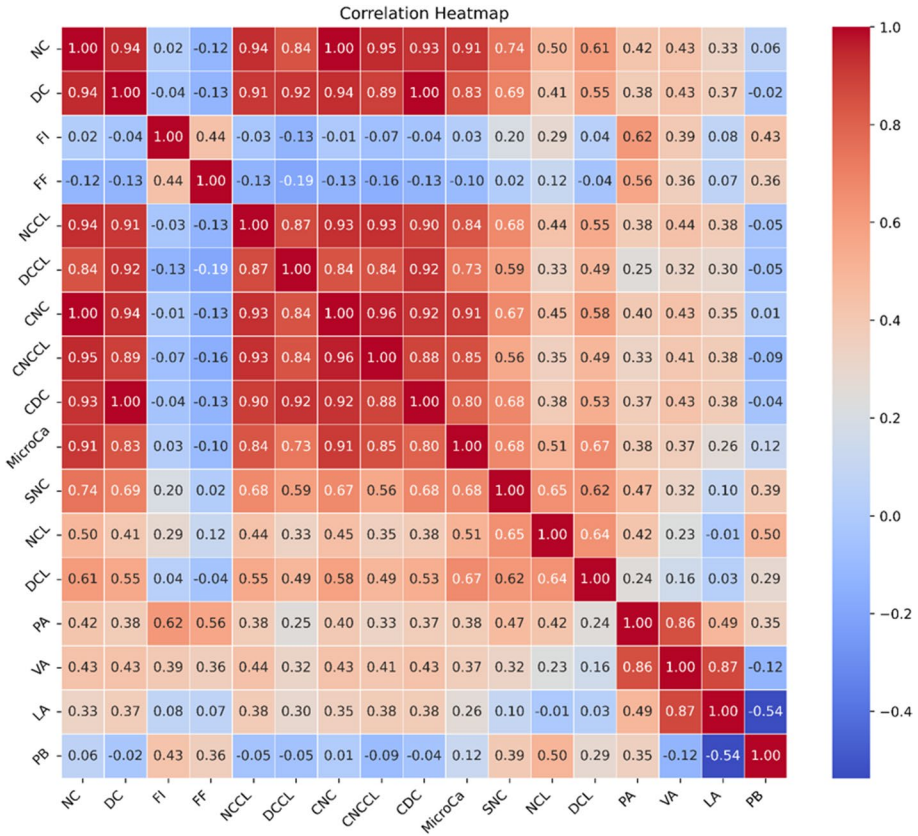


Fig. 19 Correlation heatmap of VH-IVUS features

kernels: linear, Radial Basis Function (RBF), polynomial, and sigmoid. In this experiment, SVM with RBF kernel is used for classification. The C value and γ set to train the SVM model. The VH-IVUS features are split into 70% for train and 30% for test. Table 8 displays the result of SVM classification for VH-IVUS features. Three set of parameters

Table 8 Result of SVM classification for VH-IVUS features

Plaque	Parameters	Accuracy	Sensitivity	Specificity	Precision	F1
PIT	<i>RBF-P1</i>	98.58	100	94.44	98.13	99.05
	<i>RBF-P2</i>	98.11	100	92.59	97.53	98.75
	<i>RBF-P3</i>	97.16	99.36	90.74	96.91	98.12
TCFA	<i>RBF-P1</i>	98.11	85.71	100	100	92.30
	<i>RBF-P2</i>	97.64	85.71	99.45	96.00	90.56
	<i>RBF-P3</i>	97.64	85.71	99.45	96.00	90.56
CaTCFA	<i>RBF-P1</i>	99.52	100	99.46	96.29	98.11
	<i>RBF-P2</i>	99.52	96.15	100	100	98.03
	<i>RBF-P3</i>	99.52	96.15	100	100	98.03

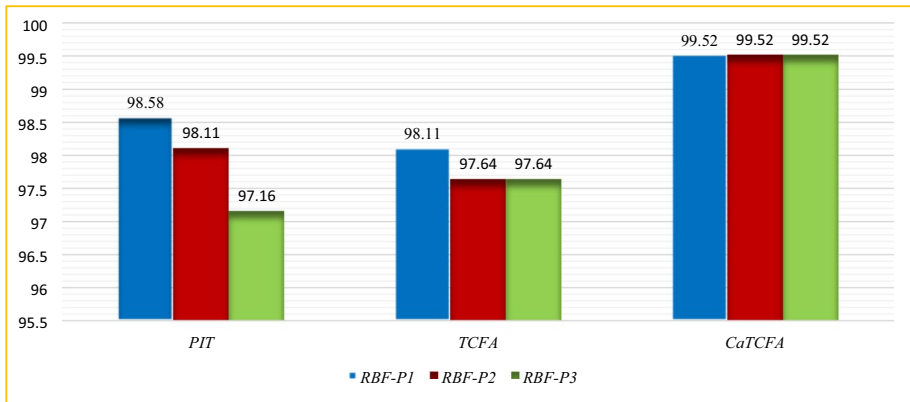


Fig. 20 Compares the accuracy for PIT, TCFA, and CaTCFA

Table 9 Result of SVM classification for VH-IVUS and IVUS features with RBF kernel

Features	Accuracy	Sensitivity	Specificity	Precision	F1
VH-IVUS	98.23	98	100	86.66	92.85
IVUS	97.34	97.0	100	81.25	89.65

were considered for this experiment includes $RBF-P1 = \{\gamma = 0.001, C = 1000\}$, $RBF-P2 = \{\gamma = 0.001, C = 10,000\}$, and $RBF-P3 = \{\gamma = 0.001, C = 100,000\}$.

Based on the above table, the result of PIT and TCFA classification for $RBF-P1$ is higher than the obtained accuracy when the C increases. However, CaTCFA achieved similar accuracy for three experiments. Its sensitivity and F1 in the first experiment are higher than the other results. However, the specificity and precision of CaTCFA show lower results than in experiment two, and the highest accuracy value was obtained by CaTCFA. Figure 20 compares the accuracy for PIT, TCFA, and CaTCFA. As shown in this figure, PIT achieved the minimum accuracy using $RBF-P3$, while achieving the best accuracy using $RBF-P1$. TCFA obtained similar results for $RBF-P2$ and $RBF-P3$, which are lower than $RBF-P1$. However, CaTCFA achieved the same result for three experiments with the highest value among the other classes.

In the next experiment, two classes were considered: TCFA and non-TCFA. VH-IVUS and IVUS features were used for classification. The classification results are shown in Table 9.

Based on the obtained results, the VH-IVUS images achieved better results than the IVUS. Some sample tests of VH-IVUS images were selected to classify TCFA and non-TCFA, their features were extracted, and the trained model predicted their labels. Table 10 shows the results of TCFA detection for VH-IVUS test images and their equivalent IVUS images.

The Receiver Operating Characteristic (ROC) curve evaluates the classification performance [29]. Sensitivity and specificity are commonly used to measure the effectiveness of binary classifier algorithms. The ROC chart combines these indicators and shows them as a single curve. The ratio of the True Positive Rate (TPR) on the vertical and False Positive Rate (FPR) on the horizontal axis is displayed in the ROC curve. Data is usually separated into a training set to create the model and a test set to check the efficiency of the model. The

Table 10 TCFA detection by SVM

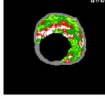

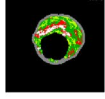

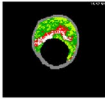

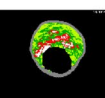

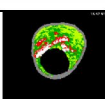

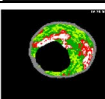

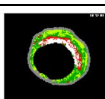

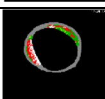

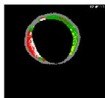

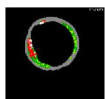


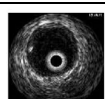
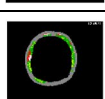

VH-IVUS image	IVUS image	SVM result
		TCFA
		TCFA
		non-TCFA
		TCFA
		TCFA
		TCFA
		TCFA
		non-TCFA
		non-TCFA
		non-TCFA
		non-TCFA
		non-TCFA

Table 11 Execution time

Parameters	k	Execution time(second)
RBF-P1	5	2.2971
	10	2.9222
RBF-P2	5	2.3362
	10	3.0068
RBF-P3	5	2.3183
	10	2.9881

training data set can be randomly divided into k folds. The $k-1$ parts are used as training data sets, and one for validation sets. The kfold cross-validation was performed with $k=5$, and the ROC curve is displayed in Fig. 21. This figure shows that the best AUC is achieved in fold 2.

4.5 Execution time

Two different values for k , 5 and 10, were considered for running the SVM with RBF-P1, RBF-P2, and RBF-P3. The execution time was calculated and displayed in Table 11. Based on this table, $k=5$ for RBF-P1 ran faster than other experiments. The longest time was obtained with $k=10$ for *RBF-P2*.

5 Discussion and conclusion

Vulnerable plaque detection and prediction are essential to prevent heart disease risk. This study proposed a new approach for plaque border detection, segmentation, feature extraction, and plaque type classification. A new, fast, and accurate algorithm was proposed for determining the borders of lumen and plaque in VH-IVUS images. However, the user should define the initial points of the level-set algorithm. In addition, accurately determining the percentage of each plaque component and necrotic pixels adjacent to the lumen was done. During the initial investigations, some segmentation algorithms, such as graph cut, were utilized to segment VH-IVUS images. However, these methods were inaccurate due to overlapping pixels on the edge of the borders of plaque components. After further research, a new semi-supervised method was suggested that precisely segments the pixels. Based on the experiments, there are better methods than clustering algorithms for achieving robust and accurate segmentation of overlapped tissue types of VH-IVUS images. Although the FCMPSO and KMPSO models achieve better results than the clustering algorithm, the problem of merging low-density clusters still needs to be solved. Furthermore, these models must set the exact number of tissue classes in VH-IVUS images. Semi-supervised models are adapted to segment the VH-IVUS images to address these limitations. Combining FCM clustering with supervised models proved more efficient in delineating the plaque components. Despite difficulties distinguishing between NC with DC and FF with FI, the FCM-SNP model can discriminate effectively between these classes. According to the different experiments conducted based on the various accurate data, the FCM-SNP model achieved the appropriate result of SW. IVUS is performed to obtain more precise information about the size and type of plaques formed inside the coronary arteries than

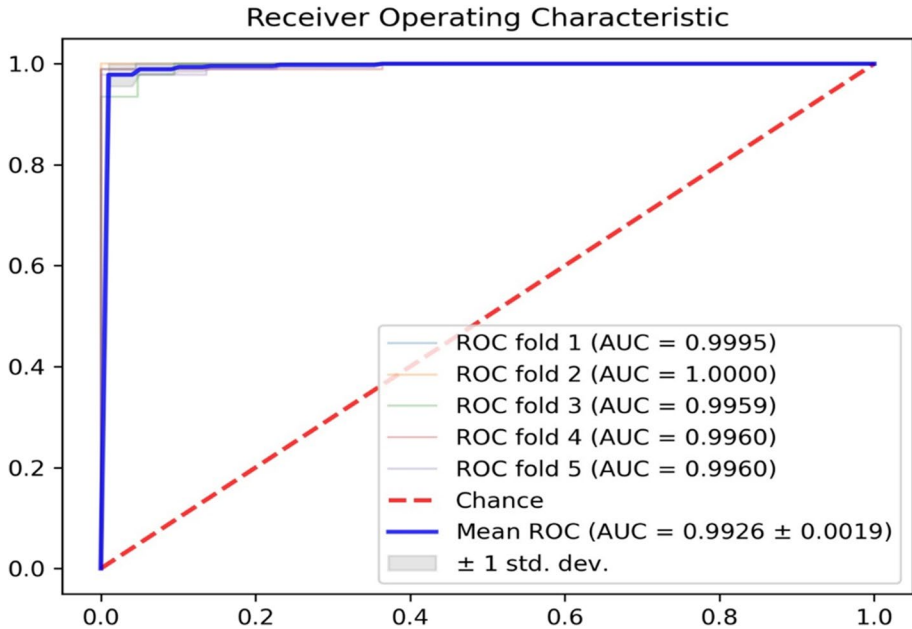


Fig. 21 ROC for five fold cross validation

angiography. However, shadow areas can be formed behind the calcium plaques, which affect segmentation accuracy and should be removed. The IVUS image segmentation uses a new hybrid level set and FCM algorithms approach. Deep learning-based methods such as Unet can also segment the IVUS images. However, a lot of IVUS data is needed to train the models. Furthermore, mask images must be produced to complete the learning process. In future work, data augmentation can increase the volume of data considered, and the Unet model can be used for IVUS image segmentation. To analyze the IVUS images for medical diagnosis, texture features in the plaque area can be extracted. These features are crucial for identifying the nature of the plaque. Earlier, we extracted such features from VH-IVUS images and achieved good results by combining them with the geometric features. Moreover, converting images to polar space has a more significant impact on plaque recognition. It's important to mention that there are several types of plaques, including TCFA, ThCFA, CaTCFA, PIT, FP, and FC. However, patient data and images of different plaque types are limited. Therefore, three plaque types were considered: PIT, TCFA, and CaTCFA. In the next experiment, we divided them into TCFA and non-TCFA. Therefore, the classification result for other classes was not obtained. Although there are some limitations, this study combines the features of IVUS and VH-IVUS images to detect the TCFA plaque accurately. The segmentation of both VH-IVUS and IVUS images is precisely performed. Additionally, the geometric features of both types of images are extracted and combined linearly. A semi-supervised hybrid method is proposed to accurately identify areas of overlapping plaque components in VH-IVUS images. In the future, OCT images will enhance reliability by combining the features of IVUS, VH-IVUS, and OCT images.

Funding Not applicable.

Data Availability The data set is not available.

Declarations The authors declare that no funds, grants, or other support were received during the preparation of this manuscript.

Conflict of Interest The authors declare no conflict of interest.

Ethical Approval Not applicable.

Competing interests Not applicable.

References

- Acharya UR, Faust O, Molinari F, Sree SV, Junnarkar SP, Sudarshan V (2015) Ultrasound-based tissue characterization and classification of fatty liver disease: A screening and diagnostic paradigm. *Knowl-Based Syst* 75:66–77
- Acharya UR, Fujita H, Sudarshan VK, Sree VS, Eugene LWJ, Ghista DN, San Tan R (2015) An integrated index for detection of Sudden Cardiac Death using Discrete Wavelet Transform and nonlinear features. *Knowl-Based Syst* 83:149–158
- Alam J, Hassan M, Khan A, Chaudhry A (2015) Robust fuzzy RBF network based image segmentation and intelligent decision making system for carotid artery ultrasound images. *Neurocomputing* 151:745–755
- Aliabadian A (2013) A Robust Clustering Approach Based on KNN and Modified C-Means Algorithm. *World Appl Sci J* 25(4):585–591
- Arumugadevi S, Seenivasagam V (2015) Comparison of clustering methods for segmenting color images. *Indian J Sci Technol* 8(7):670–677
- Athanasίου LS, Karvelis PS, Tsakanikas VD, Naka KK, Michalis LK, Bourantas CV, Fotiadis DI (2012) A Novel Semiautomated Atherosclerotic Plaque Characterization Method Using Grayscale Intravascular Ultrasound Images: Comparison With Virtual Histology. *Inf Technol Biomed, IEEE Trans* 16(3):391–400
- Benaichouche A, Oulhadj H, Siarry P (2013) Improved spatial fuzzy c-means clustering for image segmentation using PSO initialization, Mahalanobis distance and post-segmentation correction. *Digital Signal Processing* 23(5):1390–1400
- Bezdek JC, Ehrlich R, Full W (1984) FCM: The fuzzy c-means clustering algorithm. *Comput Geosci* 10(2–3):191–203
- Chang C-C, Lin C-J (2011) LIBSVM: a library for support vector machines. *ACM Trans Intell Syst Technol (TIST)* 2(3):27
- Chi D, Cheng W (2010) A Hybrid Clustering Method for Automatic Medical Image Segmentation. *Journal of Computational Information Systems* 6:1983–1993
- Chitade AZ, Katiyar S (2010) Colour based image segmentation using k-means clustering. *Int J Eng Sci Technol* 1(2):5319–5325
- Dong G, Xie M (2005) Color clustering and learning for image segmentation based on neural networks. *IEEE Trans Neural Networks* 16(4):925–936
- El-Dahshan E-SA, Mohsen HM, Revett K, Salem A-BM (2014) Computer-aided diagnosis of human brain tumor through MRI: A survey and a new algorithm. *Expert Syst Appl* 41(11):5526–5545
- Faraji M, Cheng I, Naudin I, Basu A (2018) Segmentation of arterial walls in intravascular ultrasound cross-sectional images using extremal region selection. *Ultrasonics* 84:356–365
- Gaines P (2004) 14: accuracy, precision, mean and standard deviation. *Brolin, B*
- Guven M, Cengizler C (2014) Data cluster analysis-based classification of overlapping nuclei in Pap smear samples. *Biomed Eng Online* 13(1):1
- Jain R, Kasturi R, Schunck BG (1995) *Machine vision*, vol 5. McGraw-hill, New York, pp 309–364
- Jamshidi, O, Pilevar, AH (2013) Automatic segmentation of medical images using fuzzy c-means and the genetic algorithm. *J Comput Med*, 2013. <https://doi.org/10.1155/2013/972970>

19. Kalyani S, Swarup KS (2011) Particle swarm optimization based K-means clustering approach for security assessment in power systems. *Expert Syst Appl* 38:10839–10846
20. Katouzian A, Baseri B, Konofagou EE, Laine AF (2008, May) Texture-driven coronary artery plaque characterization using wavelet packet signatures. In: 2008 5th IEEE international symposium on biomedical imaging: from nano to macro. IEEE, pp 197–200
21. Katouzian A, Karamalis A, Sheet D, Konofagou E, Baseri B, Carlier SG, Eslami A, König A, Navab N, Laine AF (2012) Iterative self-organizing atherosclerotic tissue labeling in intravascular ultrasound images and comparison with virtual histology. *IEEE Trans Biomed Eng* 59(11):3039–3049
22. Kaur A, Singh M (2012) An overview of pso-based approaches in image segmentation. *Int J Eng Technol* 2(8):1349–1357
23. Khalid NEA, Ibrahim S, Manaf M (2011, July) Brain abnormalities segmentation performances contrasting: adaptive network-based fuzzy inference system (ANFIS) vs K-nearest neighbors (k-NN) vs fuzzy c-means (FCM). In: 15th WSEAS international conference on computers, pp 15–17
24. Krinidis S, Chatzis V (2010) A robust fuzzy local information C-means clustering algorithm. *IEEE Trans Image Process* 19(5):1328–1337
25. Lee C-Y, Lee Z-J (2012) A novel algorithm applied to classify unbalanced data. *Appl Soft Comput* 12(8):2481–2485
26. Li H, He H, Wen Y (2015) Dynamic particle swarm optimization and K-means clustering algorithm for image segmentation. *Optik-Int J Light Electron Optics* 126(24):4817–4822
27. Liu Z-G, Pan Q, Dezert J (2014) Classification of uncertain and imprecise data based on evidence theory. *Neurocomputing* 133:459–470
28. Ma S, Huang J (2007) Combining multiple markers for classification using ROC. *Biometrics* 63(3):751–757
29. Madhukumar S, Santhiyakumari N (2015) Evaluation of K-means and fuzzy C-means segmentation on MR images of brain. *The Egypt J Radiol Nuclear Med* 46(2):475–479
30. Maehara A, Cristea E, Mintz GS, Lansky AJ, Dressler O, Biro S, Templin B, Virmani R, de Bruyne B, Serruys PW (2012) Definitions and methodology for the grayscale and radiofrequency intravascular ultrasound and coronary angiographic analyses. *JACC: Cardiovascular Imaging* 5(3s1):S1–S9
31. Maini R, Aggarwal H (2010) A comprehensive review of image enhancement techniques. arXiv preprint arXiv:1003.4053
32. Markoulidakis I, Kopsiaftis G, Rallis I, Georgoulas I (2021, June) Multi-class confusion matrix reduction method and its application on net promoter score classification problem. In: Proceedings of the 14th PErvasive technologies related to assistive environments conference, pp 412–419
33. Meiburger KM, Acharya UR, Molinari F (2018) Automated localization and segmentation techniques for B-mode ultrasound images: a review. *Comput Biol Med* 92:210–235
34. Meurie C, Lebrun G, Lezoray O, Elmoataz A (2003) A comparison of supervised pixels-based color image segmentation methods. application in cancerology. *WSEAS Trans Comput* 2(3):739–744
35. Nair A, Margolis MP, Kuban BD, Vince DG (2007) Automated coronary plaque characterisation with intravascular ultrasound backscatter: ex vivo validation. *EuroIntervention: J Euro PCR in Collaboration with the Working Group on Interventional Cardiology of the European Society of Cardiology* 3(1):113–120
36. Nissen SE, Yock P (2001) Intravascular ultrasound: novel pathophysiological insights and current clinical applications. *Circulation* 103(4):604–616
37. Ouldzein, H, Elbaz, M, Roncalli, J, Cagnac, R, Carrié, D, Puel, J, Alibelli-Chemarin, M-J (2012) Plaque rupture and morphological characteristics of the culprit lesion in acute coronary syndromes without significant angiographic lesion: analysis by intravascular ultrasound. *Annales de Cardiologie et d'Angéiologie*, <https://doi.org/10.1016/j.ancard.2011.07.011>
38. Qian C, Yang X (2018) An integrated method for atherosclerotic carotid plaque segmentation in ultrasound image. *Comput Methods Programs Biomed* 153:19–32
39. Rad AE, Rahim MSM, Kolivand H, Amin IBM (2017) Morphological region-based initial contour algorithm for level set methods in image segmentation. *Multimed Tools Appl* 76(2):2185–2201
40. Rezaei, Z, Kasmuni, MD, Selamat, A, Rahim MSM, Abaei G, Kadir MRA (2015) Comparative Study of clustering algorithms in order to virtual histology (VH) image segmentation. *Jurnal Teknologi* 75(2)
41. Rezaei Z, Selamat A, Taki A, Mohd Rahim MS, Abdul Kadir MR, Penhaker M, Krejcar O, Kuca K, Herrera-Viedma E, Fujita H (2018) Thin cap fibroatheroma detection in virtual histology images using geometric and texture features. *Appl Sci* 8(9):1632
42. Rezaei Z, Selamat A, Taki A, Rahim MSM, Abdul Kadir MR (2019) Systematic mapping study on diagnosis of vulnerable plaque. *Multimed Tools Appl* 78:21695–21730

43. Rezaei Z, Selamat A, Taki A, Rahim MSM, Kadir MRA (2016) Automatic Plaque segmentation based on hybrid fuzzy clustering and k nearest neighborhood using virtual histology intravascular ultrasound images. *Appl Soft Comput* 53
44. Sakata K, Kawashiri MA, Ino H, Matsubara T, Uno Y, Yasuda T, Miwa K, Kanaya H, Yamagishi M (2012) Intravascular ultrasound appearance of scattered necrotic core as an index for deterioration of coronary flow during intervention in acute coronary syndrome. *Heart Vessel* 27:443–452
45. Sankari L, Chandrasekar C (2011) Semi supervised image segmentation by optimal color seed selection using fast genetic algorithm. *Int J Computer Appl* 26(10):13–18
46. Simi V, Joseph J (2015) Segmentation of Glioblastoma Multiforme from MR Images—A comprehensive review. *The Egyptian J Radiol Nuclear Med* 46(4):1105–1110
47. Taki A (2010) Improvement and automatic classification of IVUS-VH (Intravascular Ultrasound–Virtual Histology) Images. Doctoral dissertation, Technische Universität München
48. Taki, A., Roodaki, A., Setarehdan, S. K., Avansari, S., Unal, G., & Navab, N. (2013). An IVUS image-based approach for improvement of coronary plaque characterization. *Comput Biol Med* 43(4):268–280
49. Tan KS, Isa NAM, Lim WH (2013) Color image segmentation using adaptive unsupervised clustering approach. *Appl Soft Comput* 13(4):2017–2036
50. Tan KS, Lim WH, Isa NAM (2013) Novel initialization scheme for Fuzzy C-Means algorithm on color image segmentation. *Appl Soft Comput* 13(4):1832–1852
51. Tlig L, Sayadi M, Fnaiech F (2012) A new fuzzy segmentation approach based on S-FCM type 2 using LBP-GCO features. *Signal Processing: Image Communication* 27(6):694–708
52. Wang X-Y, Wang T, Bu J (2011) Color image segmentation using pixel wise support vector machine classification. *Pattern Recogn* 44(4):777–787
53. Wang Z, Song Q, Soh YC, Sim K (2013) An adaptive spatial information-theoretic fuzzy clustering algorithm for image segmentation. *Comput Vis Image Underst* 117(10):1412–1420
54. Wright WE (1990) Parallelization of Bresenham’s line and circle algorithms. *Comput Graphics Appl* 10(5):60–67
55. Yang Y, Huang S (2012) Image segmentation by fuzzy c-means clustering algorithm with a novel penalty term. *Comput Inf* 26(1):17–31
56. Zhang C, Hu Y, Gu Y, Dong H (2024) Assembly accuracy prediction method of planetary gear train considering bolt-bearing-shaft-gear coupling effects. *Appl Math Model* 131:403–422
57. Zhang K, Zhang L, Song H, Zhou W (2010) Active contours with selective local or global segmentation: a new formulation and level set method. *Image Vis Comput* 28(4):668–676

Publisher’s Note Springer Nature remains neutral with regard to jurisdictional claims in published maps and institutional affiliations.

Springer Nature or its licensor (e.g. a society or other partner) holds exclusive rights to this article under a publishing agreement with the author(s) or other rightsholder(s); author self-archiving of the accepted manuscript version of this article is solely governed by the terms of such publishing agreement and applicable law.